



# Field emission from strained carbon nanotubes on cathode substrate

D. Roy Mahapatra<sup>a,\*</sup>, N. Sinha<sup>b</sup>, J.T.W. Yeow<sup>b</sup>, R. Melnik<sup>c</sup>

<sup>a</sup> Department of Aerospace Engineering, Indian Institute of Science, Bangalore 560012, India

<sup>b</sup> Department of Systems Design Engineering, University of Waterloo, Waterloo, Ont. N2L3G1, Canada

<sup>c</sup> Mathematical Modeling and Computational Sciences, Wilfrid Laurier University, Waterloo, Ont. N2L3C5, Canada

## ARTICLE INFO

### Article history:

Received 6 October 2007

Received in revised form 14 June 2008

Accepted 19 June 2008

Available online 27 June 2008

### Keywords:

Field emission  
Current density  
Carbon nanotube  
Strain  
phonon

## ABSTRACT

Experimental studies on the collective field emission from carbon nanotubes (CNTs) on metallic cathode substrate show wide variability. In this paper, we investigate several related effects, such as the relationship between the electron–phonon transport and the mechanical deformation in the CNTs. A systematically coupled model of randomly oriented CNTs in a thin film is developed. Numerical simulations are reported, which are able to reproduce several experimentally observed phenomena, such as a fluctuating field emission current, deflected CNT tips and the heating process. Examples are shown, where the electrodynamic stretching of the initially deflected CNTs can produce transients in the collective field emission current as large as  $10^3$  times the usual field emission current. Correspondingly, the tip temperature rises from 303 to 520 K within a time interval of 40 s. A 10 K variability in the maximum temperature is observed over the 0.0144–0.0202 V/nm range of the DC bias electric field. The maximum tensile stress is found to be 1.2 GPa, which is much smaller than the fracture stress.

© 2008 Elsevier B.V. All rights reserved.

## 1. Introduction

Field emission from carbon nanotube (CNT) was first reported in 1995 by three research groups [1–3]. With significant improvements in the processing techniques, the use of CNTs in the field emission devices (e.g., field emission displays, X-ray tube sources, electron microscopes, cathode-ray lamps, nanolithography systems, etc.) have been successfully demonstrated [4–6]. Field emission performance of a single isolated CNT is found to be remarkable. This is due to structural integrity, high thermal conductivity and geometry of the CNTs. Molecular dynamic studies [7] indicate that the stress at fracture of CNTs is on the order of tens of GPa and the fracture strain is greater than 10%. Thermal conductivity of CNTs is generally very high (3000 W/m K as reported in Ref. [8]), although ballistic phonon scattering and change in the C–C spacing due to mechanical deformation can reduce the thermal conductivity [9].

Theoretical and experimental studies on quantum thermal transport [9] suggest that the electronic transport, and hence the field emission current, is coupled with the thermal transport. If treated as a semiconductor nanowire [10], a CNT with the film substrate (cathode) on one end and the freely oriented CNT tip towards the other end (anode) allows the flow of both the

conduction and the valence electrons along its tubular surface. For CNTs with larger diameter, a spiral model of electron dispersion [11] adequately gives the electron density and the dynamic conductivity, and for pure CNTs with smaller diameter, a hexagonal dispersion model [11] adequately gives the electron density and the dynamic conductivity. However, for a deformed CNT, the electron density and the dynamic conductivity are likely to change significantly. As it is the case for the present problem of field emission from CNTs in a thin film, deformation is due to the electromechanical forces.

An added complexity is due to the non-local nature of the electro-mechanical forces, which is due to the interacting CNTs in a film. At the device level, the collective field emission current is found to be fluctuating, often with large spikes. Several studies have been reported, which shed some lights regarding the possibility of electrical breakdown [12,13] and thermal degradation [9,14] of isolated CNTs. In the case of multiwalled carbon nanotubes (MWNTs), it has been observed that the field emission current decreases by sharp steps, and this is due to the shell by shell breakdown of a MWNT [12]. In order to stabilize the collective field emission from a CNT based thin film, the bias voltage is often increased after certain low voltage exposure initially. This is done to achieve preferential breakdown of a small number of CNTs purposefully [13].

Under high electric field, the coupled electron–phonon transport is likely to produce temperature spikes. The temperature can be high enough to melt a CNT tip and often the substrate [9,14,15].

\* Corresponding author. Tel.: +91 80 22932419; fax: +91 80 23600134.  
E-mail address: [droymahapatra@aero.iisc.ernet.in](mailto:droymahapatra@aero.iisc.ernet.in) (D. Roy Mahapatra).

Also at a moderate temperature, structural defects may grow [14], leading to reduction in the electrical conductivity. Numerical study [14] based on a coupled model of field emission from the tip region and the thermal transport along the CNT length shows a steep transition of temperature. In view of the coupled nature of the electrical and the thermal degradation, in this paper, we extend the previously developed model [16] to include the details of the electron–phonon transport and the electrical breakdown. It has been experimentally observed that the collective field emission from CNT thin films has not only step-wise drops, but also preceding/successive rise in the form of spikes. The later aspect is attributed to the reorientation of few CNTs while the other CNTs undergo degradation. These reorientation effects are particularly observed at the initial step-wise rise in the collective current from the anode. Furthermore, very strong oscillations of the field emission current have been observed on saturation [13]. Small spikes in the current have also been observed experimentally [17], which can generally be attributed to the change in the gap between the elongated CNT tip and the anode plate, and also there is a possibly a dynamic contact of pulled up CNT tips with the anode plate when the bias voltage is very high ( $>800$  V).

In this paper, we focus on the device-level performance of CNTs in thin film. We consider CNTs grown on a metal substrate and together acting as cathode. The anode acts as the field emission current collector. Although an atomic force microscopy on a single CNT reveals the details of electrical conductivity and the thermal conductivity of an isolated CNT, however, it is difficult to perform such measurements for an array of interacting CNTs in a film during field emission. A major concern here is the inherent coupling among (i) the ballistic electron–phonon transport and (ii) electrostatic and electrodynamic forces causing deformation of the CNTs.

## 2. Model formulation

The current density ( $J$ ) due to field emission from a metallic surface is usually obtained by using the Fowler–Nordheim equation [18], which can be expressed as

$$J = \frac{BE^2}{\Phi} \exp\left(-\frac{C\Phi^{3/2}}{E}\right), \quad (1)$$

where  $E$  is the electric field,  $\Phi$  the work function for the cathode material,  $B$  and  $C$  are constants. The work functions for field-emission from CNT was experimentally reported at an early stage of research on this subject by Sinitsyn et al. [19], Obratsov et al. [20] and several other researchers (see e.g., Ref. [21]). In several references therein and also in the subsequent studies discussed in Section 1, it has been explained how the experimentally obtained work function values can be employed in the Fowler–Nordheim (F–N) equation. Also, it may be recalled that the F–N equation does approximate a one-dimensional transport of electron across an interface between a crystalline phase and vacuum. One limitation is that the thermal electrons, which are emitted from CNTs even at low temperatures are not accounted in a coupled manner in the theory behind the F–N equation. In the present paper, the authors have attempted to bridge these gaps by introducing thermal effect without solving a computationally intensive fully coupled quantum-mechanical problem.

In the CNT thin film problem, under the influence of sufficiently high voltage at ultra-high vacuum, the electrons emitted from the CNTs (mainly from the tip region) reach the anode. Unlike the metallic emitters, here, the surface of the cathode consists of nanostructured tubes. Also, certain amount of impurities and carbon clusters may be present. Moreover, the CNTs undergo

reorientation due to electromechanical interactions with the neighboring CNTs during field emission. Analysis of these processes requires determination of the current density by considering the CNT ensemble geometry, their dynamic orientations and the variation in the electric field during electronic transport.

### 2.1. CNT geometry and orientation

We consider an array of CNTs as shown schematically in Fig. 1. For modelling purpose, we consider a representative volume ( $V_{\text{cell}}$ ), which contains several CNTs with a prescribed distribution of their spacing on the substrate and random distribution of their curved shapes. We treat each CNT as a cylindrical nanowires by neglecting its torsional and the radial deformations and then discretize each of them into several segments with nodes. At each node, we assign the quantities of interest, such as displacement, electron density, electric field and temperature. In what follows, the governing equations involving these quantities of interest are derived systematically. An initial description of the thin film is prescribed in terms of the tip angles and the curved shapes of the CNTs in each  $V_{\text{cell}}$ , uniform conduction electron density of unstrained CNTs, a bias electric field and a reference temperature (temperature of the substrate).

Considering the previously developed phenomenological model of degradation of CNTs [16], let us assume that the number of carbon atoms formed per unit volume from a CNT is  $n_1(t)$ . Here  $t$  denotes the time. If  $\Delta h$  is the decrease in the length of the CNT over a time interval  $\Delta t$  due to degradation and if  $d_t$  is the average diameter of the CNT, then the surface area of the CNT decreases by  $\pi d_t \Delta h$ . By using the geometry details of the CNT, the decreased surface area can be expressed as

$$\pi d_t \Delta h = V_{\text{cell}} n_1(t) [s(s - a_1)(s - a_2)(s - a_3)]^{1/2}, \quad (2)$$

where  $a_1, a_2, a_3$  are the hexagonal lattice constants,  $V_{\text{cell}}$  the representative volume element and  $s = 1/2(a_1 + a_2 + a_3)$ . The chiral vector for a CNT is expressed as

$$\vec{C}_h = n\vec{a}_1 + m\vec{a}_2, \quad (3)$$

where  $n$  and  $m$  are integers ( $n \geq |m| \geq 0$ ) and the pair  $(n, m)$  defines the chirality of the CNT. By using the fact that  $\vec{a}_1 \cdot \vec{a}_1 = |a_1|^2$ ,  $\vec{a}_2 \cdot \vec{a}_2 = |a_2|^2$ , and  $2\vec{a}_1 \cdot \vec{a}_2 = |a_1|^2 + |a_2|^2 - |a_3|^2$ , the circumference and the diameter of a CNT can be expressed as [22], respectively,

$$|\vec{C}_h| = \sqrt{n^2 a_1^2 + m^2 a_2^2 + nm(a_1^2 + a_2^2 - a_3^2)}, \quad d_t = \frac{|\vec{C}_h|}{\pi}. \quad (4)$$

By defining the rate of degradation of CNT as  $v_{\text{burn}} = \lim_{\Delta t \rightarrow 0} \Delta h / \Delta t$ , dividing both sides of Eq. (2) by  $\Delta t$  as  $\lim t \rightarrow 0$ , we have

$$\pi d_t v_{\text{burn}} = V_{\text{cell}} \frac{dn_1(t)}{dt} [s(s - a_1)(s - a_2)(s - a_3)]^{1/2}. \quad (5)$$

Simplification of Eq. (4) with the help of Eq. (5) leads to the following.

$$v_{\text{burn}} = V_{\text{cell}} \frac{dn_1(t)}{dt} \left[ \frac{s(s - a_1)(s - a_2)(s - a_3)}{n^2 a_1^2 + m^2 a_2^2 + nm(a_1^2 + a_2^2 - a_3^2)} \right]^{1/2}. \quad (6)$$

Therefore, at a given time, the length of a CNT can be expressed as  $h(t) = h_0 - v_{\text{burn}} t$ , where  $h_0$  is the initial average height of the CNTs (see Fig. 1).

## 2.2. Electric field

In the absence of electronic transport within a CNT and field emission from its tip, the background electric field is simply  $E_0 = -V_0/d$ , where  $V_0 = V_d - V_s$  is the applied bias voltage,  $V_s$  the constant source potential on the substrate side,  $V_d$  the drain potential on the anode side and  $d$  is the clearance between the electrodes. The total electrostatic energy consists of a linear drop due to the uniform background electric field and the potential energy due to the charges on the CNTs. Therefore, the total electrostatic energy can be expressed as

$$\mathcal{V}(x, z) = -eV_s - e(V_d - V_s)\frac{z}{d} + \sum_j G(i, j)(\hat{n}_j - n), \quad (7)$$

where  $e$  is the positive electronic charge,  $G(i, j)$  the Green's function [23] with  $i$  indicating the ring position,  $\hat{n}_j$  describing the electron density at node position  $j$  on the ring and  $(n, m)$  representing the chirality parameters. In the present case, while computing the Green's function, we also consider the nodal charges of the neighboring CNTs. This essentially introduces non-local contributions due to the CNT distribution in the film. We compute the total electric field  $E(z) = -\nabla\mathcal{V}(z)/e$ , numerically. The effective electric field component for field emission calculation in Eq. (1) is expressed as

$$E_z = -\frac{1}{e} \frac{d\mathcal{V}(z)}{dz}. \quad (8)$$

Computation is performed at every time step, followed by update of the geometry of the CNTs. As a result, the charge distribution among the CNTs also changes and such a change affects Eq. (7). The field emission current ( $I_{\text{cell}}$ ) from the anode surface corresponding to an elemental volume  $V_{\text{cell}}$  of the film is then obtained as

$$I_{\text{cell}} = A_{\text{cell}} \sum_{j=1}^N j, \quad (9)$$

where  $A_{\text{cell}}$  is the anode surface area and  $N$  is the number of CNTs in the volume element. The total current is obtained by summing the cell-wise current ( $I_{\text{cell}}$ ).

The above formulation takes into account the effect of CNT tip orientations, and one can perform statistical analysis of the device current for randomly distributed and randomly oriented CNTs. However, due to the deformation of the CNTs under electromechanical forces, the evolution process requires a much more detailed treatment. In order to account for the changing orientations and deformation, we first estimate the effects of electromechanical forces as discussed next.

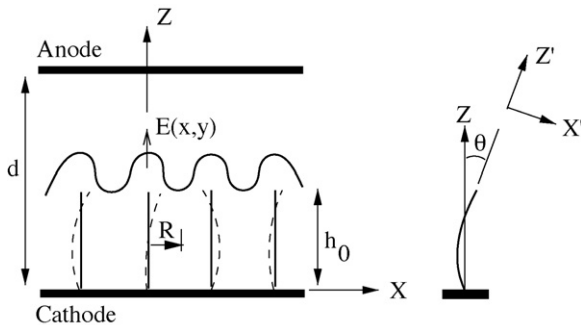


**Fig. 1.** CNT array configuration. Periodic nature of the localization of electric field  $E(x, y)$  around the tips is shown. The dotted lines indicate deformed CNTs.

## 2.3. Electromechanical forces

For each CNT, the angle of orientation  $\theta$  at its tip (see Fig. 1) is dependent on the electromechanical forces. Based on the studies reported in published literature, it is reasonable to expect that a major contribution is by the Lorentz force due to the flow of electron gas along the CNT and the ponderomotive force due to electrons in the oscillatory electric field [24]. In addition, the electrostatic force and the van der Waals force are also important.

The components of Lorentz force along  $Z$  and  $X$  directions (see Fig. 1) are approximated as

$$f_{Lz} = \pi d_t e \hat{n} E_z, \quad f_{Lx} = \pi d_t e \hat{n} E_x \approx 0. \quad (10)$$

Next, the CNT surface electron density is decomposed into a steady part (due to unstrained CNT) and a fluctuating part (due to electron–phonon interaction); that is,

$$\hat{n} = \hat{n}_0 + \hat{n}_1, \quad (11)$$

where the steady part  $\hat{n}_0$  corresponds to the Fermi level energy in an unstrained CNT, and it can be approximated as [11]

$$\hat{n}_0 = \frac{k_B T}{\pi b^2 \Delta}, \quad (12)$$

where  $k_B$  is the Boltzmann constant,  $T$  the temperature,  $b$  the interatomic distance and  $\Delta$  is the overlap integral ( $\approx 2\text{eV}$  for carbon). In Eq. (11), the fluctuating part  $\hat{n}_1$  is inhomogeneous along the length of the CNTs. Ideally,  $\hat{n}_1$  should be coupled nonlinearly with the deformation and the electromagnetic field [25]. In a simplified form, in which the circumferential mode dispersion of electron flow is neglected,  $\hat{n}_1$  is governed by the quantum-hydrodynamic equation of continuity:

$$\dot{\hat{n}}_1 + \hat{n}_0 \frac{\partial \dot{u}_z}{\partial z} = 0, \quad (13)$$

where  $u_z$  is the longitudinal displacement. In order to solve Eq. (13) for  $\hat{n}_1$ , we need to couple the equations of motion for the CNTs, which will be derived in Section 2.4. Integration of Eq. (13) with respect to time leads to the total electron density

$$\hat{n} = \hat{n}_0 \left( 1 - \int_0^t \frac{\partial \dot{u}_z}{\partial z} dt \right). \quad (14)$$

The integral in Eq. (14) is approximately the integral of strain rate over the past time history. Although computationally intensive, another way to estimate the total electron density  $\hat{n}$  is to compute the strained bond lengths as function of  $\epsilon_{zz}$  and then compute the strained band energies [10] and successively compute the Fermi-Dirac distribution. The later approach involves several theoretical issues, which have not been addressed till date in open literature. This self-consistent coupling aspect will be addressed in a forthcoming paper.

Ponderomotive force, which acts on the free charges under oscillatory electric field, tends to straighten the bent CNTs parallel to the  $z$ -axis. In order to estimate the components ( $f_{px}$ ,  $f_{pz}$ ) of the ponderomotive force (see Ref. [26]), the following approximation is made.

$$f_{pz} \approx \frac{q^2}{2m_e \omega_\tau^2} E_z \frac{\partial E_z}{\partial z}, \quad f_{px} \approx 0, \quad (15)$$

where  $q = (\pi d_t e \hat{n}) ds$  is the total charge on an elemental segment  $ds$  of a CNT,  $m_e$  the mass of an electron,  $\omega_\tau = 2\pi/\tau$  with  $\tau$  as the relaxation frequency,  $f_{pz}$  is the  $Z$  component of the ponderomotive force, while the  $X$  component  $f_{px}$  is assumed to be negligible.

We consider electrostatic force due to Coulomb interactions among the neighboring CNTs. Mechanical contact and cohesion

among the CNTs are not considered in the present model. Let us consider two small segments of the two CNTs of lengths  $ds_1$  and  $ds_2$ , respectively. The charges on these two segments are, respectively,

$$q_1 = e\hat{n}_0(\pi d_t^{(1)})ds_1, \quad q_2 = e\hat{n}_0(\pi d_t^{(2)})ds_2, \quad (16)$$

where  $d_t^{(1)}$  and  $d_t^{(2)}$  are the diameters of the two neighbouring CNTs, (1) and (2). The electrostatic force per unit length on  $s_1$  due to the entire segment  $s_2$  is given by

$$f_c = \frac{1}{4\pi\epsilon\epsilon_0} \int_0^{s_2} \frac{(\pi e\hat{n}_0)^2 d_t^{(1)} d_t^{(2)}}{r_{12}^2} ds_2, \quad (17)$$

where  $\epsilon\epsilon_0$  denotes the effective permittivity of the aggregate of CNTs and carbon clusters and  $r_{12}$  is the effective distance between the centroids of the segments  $ds_1$  and  $ds_2$ . The differential of the force  $df_c$  acts along the line joining the centroids of the segments  $ds_1$  and  $ds_2$ . Therefore, the components of the force  $f_c$  in X and Z directions are, respectively,

$$\begin{aligned} f_{c_x} &= \int df_c \cos \phi = \frac{1}{4\pi\epsilon\epsilon_0} \int_0^{s_2} \frac{(\pi e\hat{n}_0)^2 d_t^{(1)} d_t^{(2)}}{r_{12}^2} \cos \phi ds_2; \\ &\equiv \frac{1}{4\pi\epsilon\epsilon_0} \sum_{j=1}^{h_0/\Delta s_2} \frac{(\pi e\hat{n}_0)^2 d_t^{(1)} d_t^{(2)}}{r_{12}^2} \cos \phi \Delta s_2, \end{aligned} \quad (18)$$

$$\begin{aligned} f_{c_z} &= \int df_c \sin \phi = \frac{1}{4\pi\epsilon\epsilon_0} \int_0^{s_2} \frac{(\pi e\hat{n}_0)^2 d_t^{(1)} d_t^{(2)}}{r_{12}^2} \sin \phi ds_2, \\ &\equiv \frac{1}{4\pi\epsilon\epsilon_0} \sum_{j=1}^{h_0/\Delta s_2} \frac{(\pi e\hat{n}_0)^2 d_t^{(1)} d_t^{(2)}}{r_{12}^2} \sin \phi \Delta s_2. \end{aligned} \quad (19)$$

Here,  $\phi$  is the angle that the force vector  $d\vec{f}_c$  makes with the X axis,  $j$  the node number, and  $\Delta s_2$  is the length of the discrete segments (assumed uniform in the present mode). The effective distance ( $r_{12}$ ) between the centroids of the segments  $ds_1$  and  $ds_2$  is obtained as

$$r_{12} = [(d_1 - l_{x_2} + l_{x_1})^2 + (l_{z_1} - l_{z_2})^2]^{1/2}, \quad (20)$$

where  $d_1$  is the spacing between the CNTs while in contact with the surface of the cathode substrate,  $l_{x_1}$  and  $l_{x_2}$  are the deflections of the segments of the two neighboring CNTs (relative deflection considering the two end nodes of each of the segments), respectively, which are parallel to the X axis. Similarly,  $l_{z_1}$  and  $l_{z_2}$  are the deflections of the two segments, which are parallel to the Z axis. The angle  $\phi$  between  $\vec{r}_{12}$  and the x-axis parallel is expressed as

$$\phi = \tan^{-1} \left( \frac{l_{z_1} - l_{z_2}}{d_1 - l_{x_2} + l_{x_1}} \right). \quad (21)$$

Next, we consider the van der Waals effect. The van der Waals force plays an important role, not only in the interaction of the CNTs with the substrate, but also in the interaction between the walls of MWNTs and CNT bundles. Under bending type deformation, the cylindrical symmetry of the CNTs are no longer preserved, leading to an axial-radial coupling [27]. For simplicity, let us restrict ourselves to a 2D situation described with respect to (X, Z) coordinate system shown in Fig. 1, and let us assume that the lateral and the longitudinal displacements of a CNT are  $u_{x'}$  and  $u_{z'}$ , respectively. Due to their large aspect ratio, it is reasonable to idealize the CNTs as one-dimensional elastic members with the following kinematics.

$$u_{z'}^{(m)} = u_{z'0}^{(m)} - r^{(m)} \frac{\partial u_{x'}^{(m)}}{\partial z'}, \quad (22)$$

where the superscript  $(m)$  indicates the  $m$ th wall of a MWNT with  $r^{(m)}$  as its radius and  $u_{z'0}$  as the center-line longitudinal

displacement. Under tensile force, bending moment and shear force, the longitudinal displacement of the cross-section of one wall relative to the cross-section of its neighboring wall can be expressed with the help of Eq. (22) as

$$\Delta_{z'}^{(m)} = u_{z'}^{(m+1)} - u_{z'}^{(m)} = r^{(m+1)} \frac{\partial u_{x'}^{(m+1)}}{\partial z'} - r^{(m)} \frac{\partial u_{x'}^{(m)}}{\partial z'}, \quad (23)$$

where  $u_{x'}^{(m)} = u_{x'}^{(m+1)} = \Delta_{x'}$  is the lateral displacement. The lateral shear stress  $\tau_{vs}^{(m)}$  can be written as

$$\tau_{vs}^{(m)} = C_{vs} \frac{\Delta_{z'}^{(m)}}{\Delta_{x'}}, \quad (24)$$

where  $C_{vs}$  is the van der Waals coefficient. Therefore, the effective shear force per unit length of a CNT can be expressed as

$$\begin{aligned} f_{vs} &= \sum_m \int_0^{2\pi} C_{vs} \frac{\Delta_{z'}^{(m)}}{\Delta_{x'}} r_{\text{eff}} d\psi, \\ \Rightarrow f_{vs} &= \sum_m \pi C_{vs} [(r^{(m+1)})^2 - (r^{(m)})^2] \frac{1}{\Delta_{x'}} \frac{\partial \Delta_{x'}}{\partial z'}, \end{aligned} \quad (25)$$

and its components in the (X-Z) coordinate system are, respectively,

$$f_{vs_z} = f_{vs} \sin \theta(t), \quad f_{vs_x} = f_{vs} \cos \theta(t). \quad (26)$$

#### 2.4. Dynamics of CNTs

Following the steps given in Section 2.3, the net force components acting on the CNTs in the (X-Z) coordinate system are calculated as

$$\vec{f} = \int (f_l + f_{vs}) ds + f_c + f_p. \quad (27)$$

We employ this form of force components while writing the conservation law.

Under the assumption of small strain and small curvature, the longitudinal strain  $\epsilon_{zz}$  and the longitudinal stress  $\sigma_{zz}$  are written as

$$\epsilon_{zz} = \frac{\partial u_{z'0}^{(m)}}{\partial z'} - r^{(m)} \frac{\partial^2 u_{x'}^{(m)}}{\partial z'^2} + \alpha \Delta T(z'), \quad \sigma_{zz} = E' \epsilon_{zz}, \quad (28)$$

where  $E'$  is the effective modulus of elasticity,  $\Delta T(z') = T(z') - T_0$  the difference between the absolute temperature ( $T$ ) during field emission and a reference temperature ( $T_0$ ), and  $\alpha$  is the effective coefficient of thermal expansion. The longitudinal strain and the stress in Eq. (28) are employed in the strain energy expression. Subsequently, the kinetic energy is expressed in terms of the velocities  $\dot{u}_{x'}$  and  $\dot{u}_{z'}$ . Next, by applying the Hamilton principle, we obtain the governing equations in  $(u_{x'}, u_{z'})$  for each CNT, which can be expressed as,

$$\begin{aligned} E'A_2 \frac{\partial^4 u_{x'}^{(m)}}{\partial z'^4} + \rho A_0 \ddot{u}_{x'}^{(m)} - \rho A_2 \frac{\partial^2 \dot{u}_{x'}^{(m)}}{\partial z'^2} \\ - \sum_m \pi C_{vs} [(r^{(m+1)})^2 - (r^{(m)})^2] \frac{1}{\Delta_{x'}} \frac{\partial \Delta_{x'}}{\partial z'} \cos(\theta(z')) \\ - f_{lx'} - f_{cx'} = 0, \end{aligned} \quad (29)$$

$$\begin{aligned} -E'A_0 \frac{\partial^2 u_{z'0}^{(m)}}{\partial z'^2} - \frac{1}{2} E'A_0 \alpha \frac{\partial \Delta T(z')}{\partial z'} + \rho A_0 \ddot{u}_{z'0}^{(m)} \\ - \pi C_{vs} [(r^{(m+1)})^2 - (r^{(m)})^2] \frac{1}{\Delta_{x'}} \frac{\partial \Delta_{x'}}{\partial z'} \sin(\theta(z')) \\ - f_{lz'} - f_{cz'} = 0, \end{aligned} \quad (30)$$



where  $A_0$  is the effective cross-sectional area,  $A_2$  the second moment of cross-sectional area about Z-axis and  $\rho$  is the mass per unit length of CNT. We assume fixed boundary conditions ( $u = 0$ ) at the substrate–CNT interface ( $z = 0$ ) and free boundary conditions at the CNT tip ( $z = h(t)$ ). By solving Eqs. (29) and (30) in  $u_x$  and  $u_{x'0}$ , one can essentially quantify the effect of electrodynamic forcing on the current density fluctuation ( $n_1$ ) given in Eq. (14).

#### 2.4.1. Acoustical phonon interaction with electron gas

Eqs. (29) and (30) describe the coupled nature of the dynamics in its simplest form. It is important to analyze the fundamental mode interaction between the acoustical phonon and the two-dimensional electron gas flow along the CNT sheet. Here, we shall consider only the longitudinal acoustical phonon mode and the flow of  $\sigma$  electrons forward and backward along the nanotube. With the help of Eq. (14), we simplify Eqs. (29) and (30), and after linearization of the nonlinear terms using Eqs. (11) and (13), the homogeneous form of the longitudinal mode equation is obtained as

$$E'A_0 \frac{\partial^2 u_{x'0}}{\partial z'^2} - \rho A_0 \ddot{u}_{x'0} + \pi d_t^{(p)} e E_{z'} \hat{n}_1 + b_2 \hat{n}_1 = 0, \quad (31)$$

where  $b_2$  is a constant due to Coulomb interaction and is given by

$$b_2 = \sum_q \frac{\pi e^2 \hat{n}_0 d_t^{(p)} d_t^{(q)} \sin \phi}{2\epsilon \epsilon_0} \Delta s, \quad (32)$$

with superscript ( $p$ ) denoting the chosen CNT and the summation over  $q$  denoting the Coulombic contribution from neighboring CNTs. By assuming harmonic waveform of the field  $\hat{n}_1$  and  $u_{x'0}$ , that is,

$$\hat{n}_1(z', t) = \tilde{n}(\omega) e^{-ikz' + i\omega t}, \quad u_{x'0}(z', t) = \tilde{u}_z(\omega) e^{-ikz' + i\omega t}, \quad (33)$$

where  $\omega$  is the circular frequency and  $k$  is the longitudinal mode wave vector, and by eliminating  $\hat{n}_1$  in Eq. (31) with the help of Eq. (13), the dispersion relation is obtained as

$$k = -i\hat{n}_0 \frac{(\pi d_t^{(p)} e E_{z'} + b_2)}{2E'A_0} \pm \sqrt{-\hat{n}_0^2 \left( \frac{\pi d_t^{(p)} e E_{z'} + b_2}{2E'A_0} \right)^2 + \frac{\rho}{E'} \omega^2}. \quad (34)$$

In Eq. (34), the term within the square-root clearly shows the interplay between the acoustic mode and the electron density fluctuation due to background electric field ( $E_{z'} \approx V/d$ ) and the Coulomb potential  $b_2$ . There is a steady flow of electron when  $k = 0$ , and an amplification of acoustical phonon mode interaction when  $\text{Re}[k] \neq 0$ , that is, when

$$\omega > \hat{n}_0 \left( \frac{\pi d_t^{(p)} e E_{z'} + b_2}{2E'A_0} \right)^2 \sqrt{\frac{E'}{\rho}}. \quad (35)$$

It means that one obtains an amplification in the field emission current when an AC electromagnetic field is applied with frequency  $\omega$  such that Eq. (35) is satisfied. On the other hand, various parameters in the right hand side of inequality (35) can be estimated using spectral measurements under transient electro-magnetic bias field.

#### 2.4.2. Thermodynamics of electron–phonon interaction

During field emission, an electron flowing from the cathode substrate towards the anode along the CNT surface acquires energy and escapes from the tip region towards the anode by crossing the Fermi energy level. Thus, the thermodynamic process is similar to the thermionic emission, except that the temperature for thermionic emission is much higher than the temperature for field emission from CNTs. The energy lost in the replacement of the

emitted electron is likely to create intense temperature gradient in the emitter [28]. For a metallic cone tip with hemispherical cap having  $\approx 0.3 \mu\text{m}$  or smaller diameter, an empirical estimate of energy loss per emitted electron from the tip was reported to be  $W = \Phi + \beta k_B T$  (see Ref. [29]), where  $\Phi$  is the work function and  $\beta$  is a constant or an empirical function of temperature. On the other hand, due to particular atomic arrangement at the tip and the rolled graphene sheet in a CNT, the electrical potential across the CNT tip and hence the field emission characteristics are different than those due a metallic surface. Experimental studies using free-standing CNT shows that the temperature distribution is broadened as its length decreases [9] and most of the energy provided by the electric field to each electron is converted into phonons within the nanotube. This correlates well with the observations reported in Ref. [9] that the electron mean-free path is shorter than the umklapp scattering mean-free path for inter-phonon scattering. Thus, a diffusive thermal transport model in the ballistic regime appears suitable to analyze the temperature rise in the CNTs. In the ballistic regime, the heat flux carried away by the phonons can be obtained by integrating the non-equilibrium phonon distribution associated with several photon modes [30]. Further simplification of this integral based on the analogy with the Landauer formula for ballistic conduction of electron leads to an approximate thermal conductance quantum  $k_Q = \pi k_B^2 T / (6\hbar)$ . We employ this temperature dependent thermal conductance to derive the thermal transport model, which is discussed next. The heat flux in a CNT segment is first written as

$$dQ = I^2 \frac{\rho_c \pi d_t^2}{4L} dz', \quad (36)$$

where  $L$  is the effective length of the CNT,  $I = \pi d_t e \dot{n}$  denotes the current and  $\rho_c \approx E_{z'} l_e / (e \dot{n})$  denotes the electrical resistivity with  $l_e$  as the electron mean-free path. Considering heat conduction of the form  $q_F = -k_Q \nabla T$  and thermal radiation from the CNT, the quantum-thermal energy balance equation in rate form is expressed as

$$dQ - \frac{\pi d_t^2}{4} dq_F - \pi d_t \sigma_{SB} (T^4 - T_0^4) dz' = 0, \quad (37)$$

where  $\sigma_{SB}$  is the Stefan–Boltzmann constant.

At the substrate–CNT interface ( $z' = 0$ ), the boundary condition is  $T = T_0$ . At the CNT tip ( $z' = L$ ),  $q_F = 2Mk_Q T$  (see Ref. [9]), where  $M \approx 0.1875 k_B T d_t^2 / (\hbar a_1 c)$  and  $c \approx 1.5 \times 10^4$  m/s is the in-plane speed of sound in graphite [31]. We assume  $a_1 = a_2 = a_3$ .

Eq. (37) is discretized in  $T(z')$  using a four-point finite differencing scheme over each segment  $0 \leq z' \leq L$ . Note that in the developed model, the temperature distribution, the electron density  $\hat{n}$  and the electric field  $E_{z'}$  are strongly coupled. This means that all the respective governing equations are to be solved simultaneously. Based on Eq. (8), we first compute  $E_{z'}$  at the nodes, and then solve Eqs. (14), (29), (30) and (37) in  $(\hat{n}, u_{x'}, u_{x'}, T)$ . This is done at each time step  $t_{i+1} = t_i + \Delta t$  and the state of each CNT is updated. The angle of orientation  $\theta$  between the nodes  $j + 1$  and  $j$  at the two ends of a CNT segment of length  $\Delta s_j$  is expressed as

$$\theta(t) = \tan^{-1} \left( \frac{(x^{j+1} + u_x^{j+1}) - (x^j + u_x^j)}{(z^{j+1} + u_z^{j+1}) - (z^j + u_z^j)} \right), \quad (38)$$

$$\begin{bmatrix} u_x^j \\ u_z^j \end{bmatrix} = [\Gamma(\theta(t - \Delta t)^j)] \begin{bmatrix} u_{x'}^j \\ u_{z'}^j \end{bmatrix}, \quad (39)$$

where  $\Gamma$  is the usual coordinate transformation matrix. Most importantly, the angle at the tip of each CNT after incremental reorientation under force field is obtained using the above

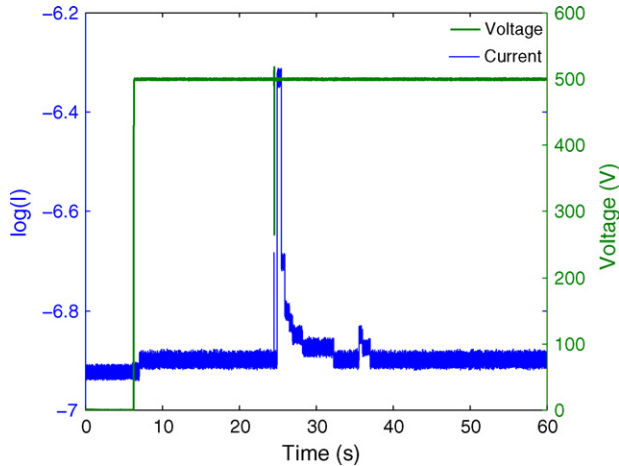


**Fig. 2.** Spikes in the field emission current at low bias voltage due to reorientation and pull-up of few CNTs.

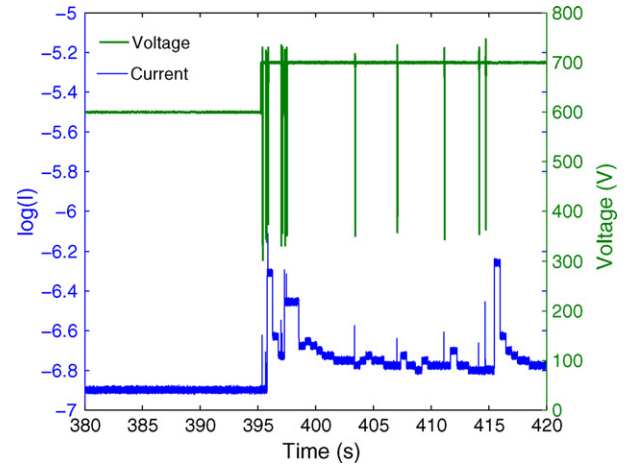


**Fig. 3.** Fluctuation of field emission current from a baked sample having vertically aligned CNTs.

equations. Field emission current at each time step is calculated based on Eq. (9).

### 3. Results and discussions

The film surface area (projected on the anode) considered here is  $49.93 \text{ mm}^2$ . The average thickness of the film is  $10\text{--}14 \text{ }\mu\text{m}$ . Actual experiments were performed in a vacuum chamber fitted with a micro-meter to control the electrode gap. Field emission current histories were measured under various DC bias voltages. The gap ( $d$ ) between the electrodes is maintained at  $34.7 \text{ }\mu\text{m}$ . Fig. 2 shows the occurrence of current spikes at 500 V (a low bias voltage) obtained experimentally and such response is an indication that few CNTs are emitting heavily and they are pulled up towards the anode. Fig. 3 shows a more number of spikes as the bias voltage is increased to 700 V. The CNTs used here were initially in the vertically aligned positions. Next, we report the results based on numerical simulations, which captures such spiking in the current.

For numerical simulations, the constants in Eq. (1) were taken as  $B = (1.4 \times 10^{-6}) \times \exp((9.8929) \times \Phi^{-1/2})$  and  $C = 6.5 \times 10^7$  (see Ref. [14]). It has been reported in the literature (e.g., Ref. [14]) that the work function  $\Phi$  for CNTs is smaller than the work functions for metal, silicon, and graphite. However, there are significant variations in the experimental values of  $\Phi$  depending on the types of CNTs. The type of substrate materials has also significant influence on the band-edge potential. The numerical results reported in this paper are based on computation with  $\Phi = 2.2 \text{ eV}$ . We solve for the mechanical displacement field ( $u$ ), electric field ( $E$ ), current density ( $n$ ) and temperature ( $T$ ) distributions in each CNT with the help of Eqs. (29) and (30), Eqs. (8), (14) and (37), respectively. They are solved in a coupled manner. Finally, the field emission current is computed using Eq. (9).

Following sample configuration details have been used: average height of CNTs  $h_0 = 12 \text{ }\mu\text{m}$ , average diameter  $d_t = 3.92 \text{ nm}$  and average spacing  $d_1 = 2 \text{ }\mu\text{m}$  at the substrate contact regions. A random initial height distribution with the range  $h = h_0 \pm 2 \text{ }\mu\text{m}$  and a random initial distribution of the orientation angle  $\theta$  at the nodes have been used. The random orientation distribution is parameterized in terms of the initially assigned tip deflection (denoted by  $h/m'$ ,  $m' > 1$ ). Several simulations were performed and the output data (time histories, etc.) were averaged. Figs. 4–6 show the simulated effects of the largely deflected CNT tips in the film (higher  $h/m'$  values) and the effects of increasing

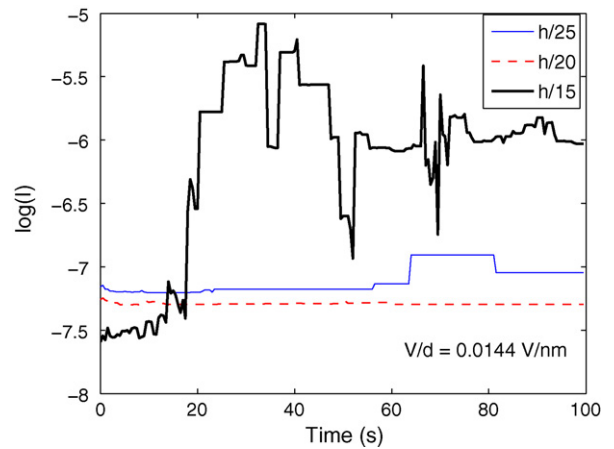


**Fig. 4.** Field emission current histories for various initial average tip deflections  $h/m'$  and under bias voltage  $V_0 = 500 \text{ V}$ .

bias voltages on the field emission current histories. By comparing the curves in these figures, the following two important observations can be drawn: (1) for a constant bias voltage, as the initial average deflections/angle of the CNTs are increased from  $h_0/25$  to  $h_0/20$ , the average current reduces. With further increase in the

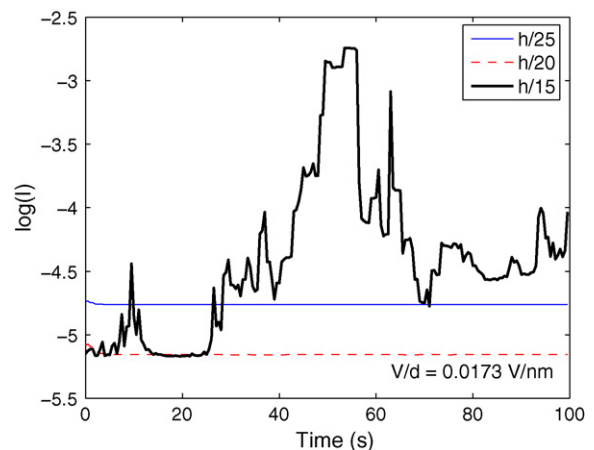


**Fig. 5.** Field emission current histories for various initial average tip deflections  $h/m'$  and under bias voltage  $V_0 = 600 \text{ V}$ .

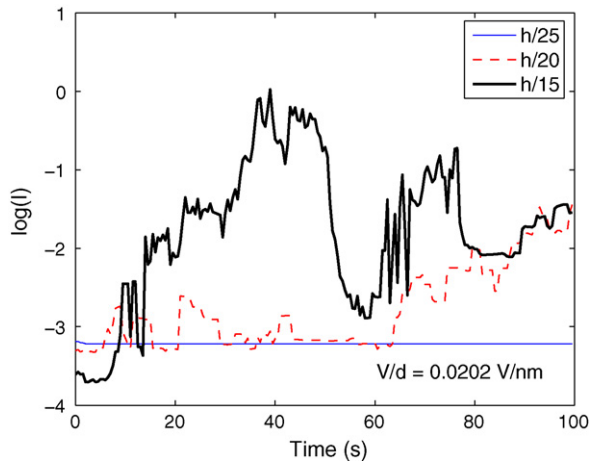


**Fig. 6.** Field emission current histories for various initial average tip deflections  $h/m'$  and under bias voltage  $V_0 = 700$  V.

initial state of deflection/angle (e.g.,  $h_0/15$ ), the electrodynamic interaction among CNTs and the mechanical deformation produces sudden stretching of the deflected tips towards the anode; (2) the trends in the current fluctuation for higher  $h_0/m'$  in Fig. 6 (for high bias) indicate current spikes with an amplitude factor of  $\approx 10^3$ , whereas in Figs. 4 and 5 (for low bias voltage) the trend indicates current spikes with an amplitude factor of  $\approx 10^2$ . The current spikes are the results of electrodynamic stretching, causing reorientation of the CNTs. Fig. 7 shows a comparison of the distribution of the tip angle  $\theta$  over an array of 100 CNTs at  $t = 0$  with  $h/20$  and  $t = 100$ s under bias voltage  $V_0 = 700$  V (0.0202 V/nm). Fig. 7 reveals that after experiencing the electrodynamic stretching, some of the CNTs with angle  $+\theta$  may reorient to  $-\theta$ , whereas some of the already largely deflected CNTs move further away with increasing  $|\theta|$  due to Coulombic repulsion. The deflected tips shown in the SEM images in Fig. 8 gives a qualitative agreement between the experiment and the simulation.

As seen in Figs. 4–6, since the current spikes can cause high stress and growth of defects in CNT, we further analyze the stress accumulated in the CNTs based on Eq. (28). It may be noted that the bias electric field ( $V/d$ ) used in the numerical simulation is much smaller than those used in the reported literature regarding degradation and breakdown of single CNT [14,17]. Usually,  $V/d > 1$  V/nm is considered to be high enough to produce defects in the CNTs. Based on the simulation, the maximum

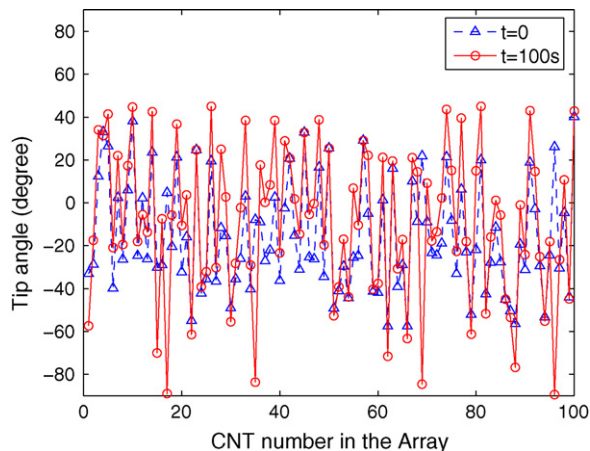


**Fig. 7.** Comparison of tip orientation angles  $\theta(t)$  at  $t = 0$  and  $t = 100$  s.

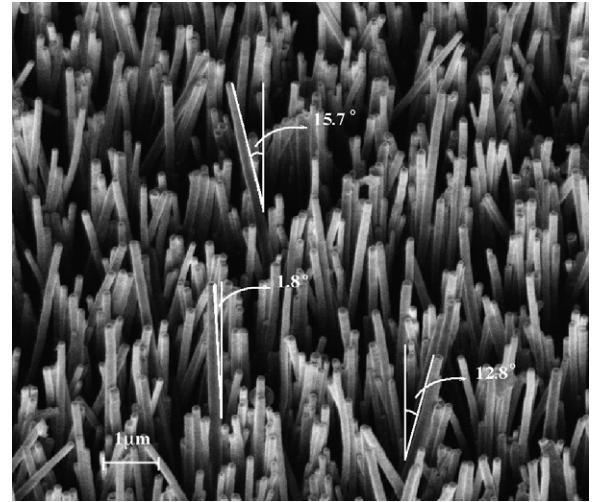


**Fig. 8.** SEM image showing the oriented tips of CNTs after  $t = 100$  s.

**Table 1**

Maximum tensile stress  $\sigma_{zz}$  (GPa) due to electro-mechanical pull-up of CNTs for various initial tip deflections and background electric field  $V_0/d$

Initial tip deflection	0.0144 V/nm	0.0173 V/nm	0.0202 V/nm
$h/25$	0.309	0.024	0.403
$h/20$	0.091	0.975	1.056
$h/15$	1.223	1.173	1.095

tensile stress attained during 100 s of field emission corresponding to Figs. 4–6 is given in Table 1. Data in this table indicate non-monotonic increase in the stress for increasing  $h/m'$ . The highest stress is observed for  $h/15$  under low bias field of 0.0144 V/nm. For higher bias field, the stress increases monotonically for increasing  $h/m'$ . The maximum stress in all the cases is found to be 1.223 GPa, which is much smaller than the fracture stress [7] ( $>65$  GPa). Therefore, it is less likely in the present case that the CNTs in the film could fail by fracture under the chosen initial film pattern and bias field. This is confirmed from Fig. 2. However, electric breakdown process is possibly accelerated as the current spikes also give rise to temperature spikes. At a breakdown temperature  $T_c$  (generally  $>900$  K), one may expect degradation of CNTs, and hence a proportional decrease in the electron density at a rate  $\hat{n}\omega_c \exp(-\Delta_c/(k_B T_c))$ , where  $\omega_c$  is the highest frequency in the spectrum of the temperature spike and

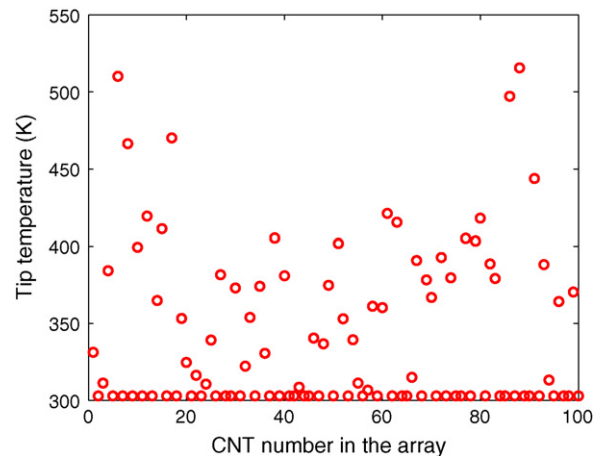


**Fig. 9.** Maximum temperature of the CNT tips during 100 s of field emission.

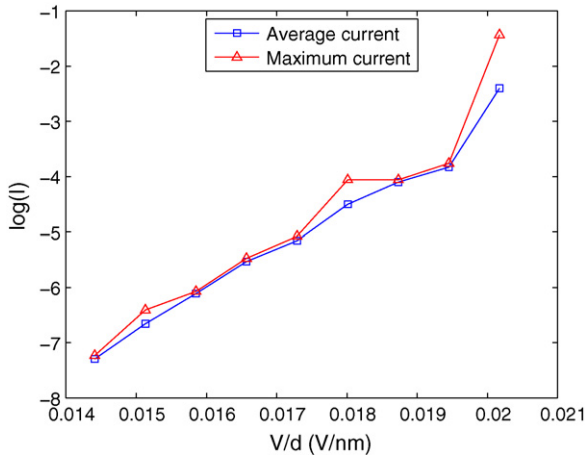


**Fig. 10.** Variation in the maximum current and the average current due to field emission under increasing bias electric field.

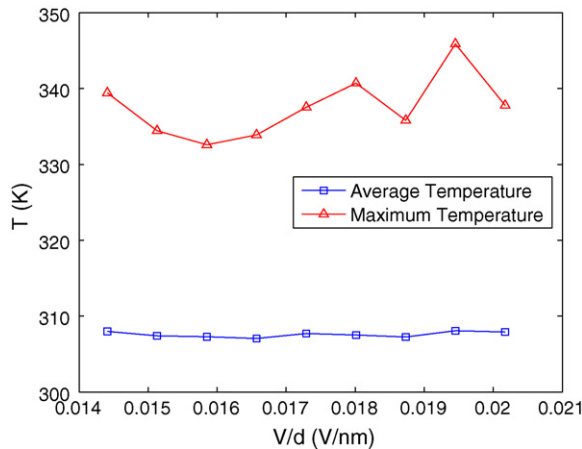


**Fig. 11.** Variation in the maximum and average temperature due to field emission under increasing bias electric field.

$\Delta_c \approx 3\text{--}4$  eV (see Ref. [9]). In Fig. 9, we plot the maximum tip temperature distribution over an array of 100 CNTs during field emission at a bias voltage of 700 V over 100 s duration (corresponding to the tip angle distribution shown in Fig. 7). This result indicates a temperature rise up to  $\approx 520$  K for a bias field of 0.0202 V/nm. This temperature rise was observed at  $t = 40$  s. Based on the statistical analysis of the simulated data, we plot the maximum current and the average current in Fig. 10 for various bias voltages. Similarly, the maximum temperature and the average temperature for various bias voltages are plotted in Fig. 11. A linear  $\log(I)$  vs.  $V/d$  behaviour can be observed in Fig. 10. However, at higher bias voltages, the maximum current tends to differ from the average current. From Fig. 11, it can be seen that the average temperature is almost independent of the bias voltage, whereas the maximum temperature fluctuates by more than 10 K over the range of bias field.

#### 4. Concluding remarks

In this paper, we have developed a method to analyze systematically the collective field emission from CNTs in a thin film, electron–phonon interaction and non-local electrodynamic effects on the CNTs. It helps in analyzing various coupled effects related to the mechanics, the thermodynamics and the process of collective field emission from the CNTs. In particular, it is shown how the electric field, the electronic transport, the mechanical deformation of the CNTs and the heat conduction in the CNTs due to ballistic phonon scattering are interrelated. Results presented along with the estimate of tensile stresses are indicative of the collective field emission performance of the CNT thin film.

#### References

- [1] A.G. Rinzier, J.H. Hafner, P. Nikolaev, L. Lou, S.G. Kim, D. Tomanek, D. Colbert, R.E. Smalley, *Science* 269 (1995) 1550–1553.
- [2] W.A. de Heer, A. Chatelain, D. Ugarte, *Science* 270 (1995) 1179–1180.
- [3] L.A. Chernozatonskii, Y.V. Gulyaev, Z.Y. Kosakovskaya, N.I. Sinitsyn, G.V. Torgashov, Y.F. Zakharchenko, E.A. Fedorov, V.P. Valchuk, *Chem. Phys. Lett.* 233 (1995) 63–68.
- [4] J.M. Bonard, J.P. Salvetat, T. Stockli, L. Forro, A. Chatelain, *Appl. Phys. A* 69 (1999) 245–254.
- [5] Y. Saito, S. Uemura, *Carbon* 38 (2000) 169–182.
- [6] H. Sugie, M. Tanemure, V. Filip, K. Iwata, K. Takahashi, F. Okuyama, *Appl. Phys. Lett.* 78 (2001) 2578–2580.
- [7] T. Belytschko, S.P. Xia, G.C. Schatz, R.S. Rouff, *Phys. Rev. B* 65 (2002) 235430.
- [8] P. Kim, L. Shi, A. Majumdar, P.L. McEuen, *Phys. Rev. Lett.* 87 (2001) 215502.
- [9] H.-Y. Chiu, V.V. Deshpande, H.W.Ch. Postma, C.N. Lau, C. Mikó, L. Forró, M. Bockrath, *Phys. Rev. Lett.* 95 (2005) 226101.
- [10] L. Yang, M.P. Anantram, J. Han, J.P. Lu, *Phys. Rev. B* 60 (1999) 13874.
- [11] G.Y. Slepian, S.A. Maksimenko, A. Lakhtakia, O. Yevtushenko, A.V. Gusakov, *Phys. Rev. B* 60 (1999) 17136–17149.
- [12] P.G. Collins, M. Hersam, M. Arnold, R. Martel, Ph. Avouris, *Phys. Rev. Lett.* 86 (2001) 3131–3182.
- [13] R.V. Seidel, A.P. Graham, B. Rajasekharan, E. Unger, M. Liebau, G.S. Duesberg, F. Kreupl, W. Hoenlein, *J. Appl. Phys.* 96 (2004) 6694–6699.
- [14] N.Y. Huang, J.C. She, J. Chen, S.Z. Deng, N.S. Xu, H. Bishop, S.E. Huq, L. Wang, D.Y. Zhong, E.G. Wang, D.M. Chen, *Phys. Rev. Lett.* 93 (2004) 075501.
- [15] L. Nilsson, O. Groening, P. Groening, L. Schlapbach, *Appl. Phys. Lett.* 79 (2001) 1036–1038.
- [16] N. Sinha, D. Roy Mahapatra, J.T.W. Yeow, R.V.N. Melnik, D.A. Jaffray, *J. Comput. Theor. Nanosci.* 4 (2007) 535–549.
- [17] J.M. Bonard, C. Klinke, K.A. Dean, B.F. Coll, *Phys. Rev. B* 67 (2003) 115406.
- [18] R.H. Fowler, L. Nordheim, *Proc. R. Soc. Lond. A* 119 (1928) 173–181.
- [19] N.I. Sinitsyn, Y.V. Gulyaev, G.V. Torgashov, L.A. Chernozatonskii, Z.Y. Kosakovskaya, Y.F. Zakharchenko, S.T. Mevlyut, O.E. Glukhova, *Appl. Surf. Sci.* 111 (1997) 145–150.
- [20] A.N. Obraztsov, A.P. Volkov, I. Pavlovsky, *Diamond Relat. Mater.* 9 (2000) 1190–1195.
- [21] Y. Chen, S.Z. Deng, N.S. Xu, J. Chen, X.C. Ma, E.G. Wang, *Mater. Sci. Eng. A* 327 (2002) 16–19.
- [22] H. Jiang, P. Zhang, B. Liu, Y. Huang, P.H. Geubelle, H. Gao, K.C. Hwang, *Comput. Mater. Sci.* 28 (2003) 429–442.
- [23] A. Svizhenko, M.P. Anantram, *Phys. Rev. B* 72 (2005) 085430.
- [24] O.E. Glukhova, A.I. Zhanov, I.G. Torgashov, N.I. Sinitsyn, G.V. Torgashov, *Appl. Surf. Sci.* 215 (2003) 149–159.
- [25] L. Wei, Y.-N. Wang, *Phys. Lett. A* 333 (2004) 303–309.
- [26] A.L. Musatov, N.A. Kiselev, D.N. Zakharov, E.F. Kukovitskii, A.I. Zhanov, K.R. Izrael'yants, E.G. Chirkova, *Appl. Surf. Sci.* 183 (2001) 111–119.
- [27] R.S. Ruoff, J. Tersoff, D.C. Lorents, S. Subramoney, B. Chan, *Nature* 364 (1993) 514–516.
- [28] W.W. Dolan, W.P. Dyke, J.K. Trolan, *Phys. Rev.* 91 (1953) 1054–1057.
- [29] W.B. Nottingham, *Phys. Rev.* 59 (1941) 906.
- [30] T. Yamamoto, S. Watanabe, K. Watanabe, *Phys. Rev. Lett.* 92 (2004) 075502.
- [31] M.S. Dresselhaus, G. Dresselhaus, P.C. Eklund, *Science of Fullerenes and Carbon Nanotubes*, Academic Press, NY, 1996.